

# Leveraging Multi-Primary PS-InSAR Configurations for the Robust Estimation of Coastal Subsidence

Stacey A. Huang<sup>1</sup>, Member, IEEE, and Jeanne M. Sauber

**Abstract**—Interferometric synthetic aperture radar (InSAR) is a key technique used to constrain contributions of diverse processes to coastal subsidence, also known as vertical land motion (VLM). However, coastal environments can pose major challenges for InSAR due to natural disturbances that degrade interferogram quality. We describe a new multi-primary pairing strategy for persistent scatterer InSAR (PS-InSAR) to estimate subsidence in challenging coastal environments. Our method retains only consistent PS candidates across multi-primary sub-stacks and solves for redundant velocity observations using SVD-based inversion, similar to the conventional small baseline subset (SBAS) method. Through simulations and a case study comparing with single-primary PS-InSAR and conventional SBAS techniques, we show that our pairing strategy reduces temporal and spatial uncertainty in subsidence estimates in the presence of strong but temporary decorrelation loss, even with increased distance from the reference point. Moreover, our method visibly dampens time-series variation and decreases standard error in our time-series fit by nearly 2x in our case study. Thus, we find that implementing a multi-primary PS-InSAR configuration is a simple method of increasing the robustness of VLM estimates in challenging coastal environments.

**Index Terms**—Coastal subsidence, persistent scatterer (PS-InSAR), sea level rise, vertical land motion (VLM).

## I. INTRODUCTION

COASTAL subsidence is a major issue that accelerates the hazards of sea level rise in many areas around the world. Interferometric synthetic aperture radar (InSAR) is a well-established spaceborne geodetic technique for characterizing the severity and extent of coastal subsidence with high spatial resolution, a strong complement to sensors such as GPS/GNSS and tide gauge stations with denser temporal sampling [1], [2]. Using these data to identify local and regional trends in subsidence enables decision-makers to develop the most effective resilience measures for the local population. However, obtaining meaningful measurements with InSAR can be difficult over small, heavily vegetated tropical islands, limiting valuable measurements of local subsidence patterns over many landmasses which are known to subside at rates

Manuscript received 8 September 2023; revised 5 January 2024; accepted 23 January 2024. Date of publication 25 January 2024; date of current version 7 February 2024. This work was supported by the National Aeronautics and Space Administration (NASA) Postdoctoral Program Fellowship (NPP) currently administered by the Oak Ridge Associated Universities (ORAU), and previously administered by the University Space Research Association (USRA) until January 2022, and NASA’s “Coastal land change due to earthquakes and implications for sea-level rise in the Samoan Islands under Grant 19-ESI19-0027.” (Corresponding author: Stacey A. Huang.)

The authors are with the NASA Goddard Space Flight Center, Greenbelt, MD 20771 USA (e-mail: stacey.a.huang@nasa.gov).

Digital Object Identifier 10.1109/LGRS.2024.3358737

higher than the global average [3]. The small surface area of these islands also hinders the effectiveness of standard methods to combat strong decorrelation, including multilooking and filtering.

In such environments, persistent scatterer InSAR (PS-InSAR) can be a strong alternative. PS-InSAR techniques process scenes at full resolution and analyze only strong, nondecorrelating, point-like scatterers [4], [5]. Still, coastal environments can introduce challenges for PS-InSAR due to events such as storm surges, flooding, and heavy rains that can result in temporary or long-term changes in the position and scattering characteristics of potential PS, effectively reducing the number of true PS. These disruptions can also lead to noisy and biased subsidence estimates that can be difficult to systematically correct across many of thousands of PS. Despite these limitations, PS-InSAR analysis techniques remain the most viable option for challenging coastal environments compared with non-PS methods because PSs are resistant to all other forms of decorrelation. In this letter, we present a method of reducing the spatial and temporal uncertainties in the presence of strong but temporary decorrelation using multi-primary pairing strategies for PS-InSAR interferogram generation. Our work extends upon previous studies that have only, until now, empirically demonstrated the benefit of multi-primary configurations. In particular, we explicitly address the theoretical basis for a multi-primary configuration and apply our findings to a specific context: coastal PS decorrelation. Within that context, we also directly examine the relationship of the number of primary images used with the resulting error. Our findings demonstrate a robust, easy-to-implement method for improving estimates of vertical land motion (VLM) along coasts worldwide using InSAR.

## II. BACKGROUND AND THEORY

### A. Modeling InSAR-Derived VLM Uncertainty

To estimate deformation velocities from InSAR measurements, we solve a linear equation in the form [6]

$$\begin{aligned} Av &= \Phi \\ v &= A^+ \Phi \end{aligned} \quad (1)$$

where  $A$  is an  $m \times n$  matrix, given the number of interferometric pairs  $m$  and number of total scenes  $n$ ,  $v$  is defined as an  $n \times 1$  velocity vector, and  $\Phi$  is an  $m \times 1$  matrix that contains the observed interferometric phases, i.e.,  $\Phi_{i,j} = \phi_i - \phi_j$ . The entries of  $A$  are defined as the time difference between

acquisitions in the chosen scene pair, e.g.,  $A_{i,j} = t_j - t_i$  between the phase observations  $i$  and  $j$ ; we assume that  $j > i$ . The  $+$  operator denotes the Moore–Penrose inverse.

We can generalize (1) to explicitly take into account the role of interferometric pair selection given a fixed set of SAR scenes. Suppose that  $k$  is the total number of unique interferometric pairs that can be formed given the number of scenes  $n$ , such that  $k = (n!)/(2(n-2)!)$ . Next suppose that  $A = CA_{\text{all}}$  and  $\Phi = C\Phi_{\text{all}}$  so that (1) becomes

$$\begin{aligned} CA_{\text{all}}v &= C\Phi_{\text{all}} \\ v &= A_{\text{all}}^+ C^+ C\Phi_{\text{all}} \end{aligned} \quad (2)$$

where  $C$  is a logical combination matrix with dimensions  $m \times k$  and 1's in the columns and rows corresponding to observed interferograms and 0's otherwise.  $A_{\text{all}}$  is a  $k \times n$  matrix containing the time differences between all possible interferometric pairs, and  $\Phi_{\text{all}}$  is a  $k \times n$  matrix containing the phases of all possible interferometric pairs.  $A_{\text{all}}$  and  $\Phi_{\text{all}}$  are fixed for a given set of scenes;  $C$  changes based on the interferometric pairs chosen for analysis.

From (2), the uncertainty in the estimated velocities from interferometric measurements can then be written in terms of the uncertainty of  $v$

$$\begin{aligned} rCICov(v) &= A_{\text{all}}^+ C^+ C Cov(\Phi_{\text{all}}) (C^+ C)^T (A_{\text{all}}^+)^T \\ &= A_{\text{all}}^+ C^+ C Cov(\Phi_{\text{all}}) C^+ C (A_{\text{all}}^+)^T \end{aligned} \quad (3)$$

where  $Cov(\Phi_{\text{all}})$  is the interferometric covariance. The entries of the interferometric covariance matrix can be written as [7]

$$\text{cov}(\phi_{i,j}, \phi_{k,l}) = \gamma(\phi_{i,j}, \phi_{k,l}) \sigma_{i,j} \sigma_{k,l}. \quad (4)$$

Here,  $\gamma(\phi_{i,j}, \phi_{k,l})$  is the interferometric correlation coefficient, and  $\sigma_{i,j}$  and  $\sigma_{k,l}$  are the interferometric variances. Often, instead of the velocity  $v$ , we consider the cumulative displacement  $d$ , given by

$$d = \sum_i v_i \Delta t_i \quad (5)$$

with the corresponding uncertainty

$$\sigma_d = \sqrt{\sum_i \sum_j \text{cov}(v_{i,j})(t_j - t_i)^2} \quad (6)$$

where  $\sigma_d$  is the standard deviation of  $d$ , and  $\text{cov}(v_{i,j})$  contains the entries of the covariance matrix of  $v$ . Examining (6), we can see that the covariance of  $d$  is a linear combination of the covariances of the chosen interferometric scenes, which depends on the interferometric correlation coefficient and the individual interferometric variances. Reducing the value of  $\sigma_d$  requires a strategic choice of  $C$  to reduce the contributions of any high-variance terms in  $Cov(\Phi_{\text{all}})$ .

### B. Interferometric Pairing Strategy

The choice of interferogram pairing strategy depends both on the characteristics of the dataset (which determines  $A_{\text{all}}^+$  and  $Cov(\Phi_{\text{all}})$ ) and on the targeted scattering mechanism, which generally falls into two main categories: point scatterers and distributed scatterers. In PS-InSAR, which optimizes for

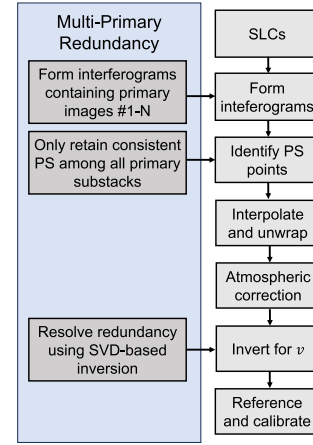


Fig. 1. Flowchart of the implemented PS-InSAR method, with the multi-primary (redundant) aspects highlighted in blue.

point-like scatterers with little temporal decorrelation, a single-primary pairing configuration is standard, where one scene is chosen as the “primary” (or “reference”), and the interferometric stack is formed by pairing all the “secondary” images with the chosen primary image. For techniques such as small baseline subset (SBAS) and its derivatives, which optimize for distributed scatterers that suffer from moderate temporal decorrelation but whose signal can be averaged to extract underlying deformation trends for effective time-series analysis, a multi-primary configuration tends to be standard. Several excellent reviews of InSAR time-series methods and their pairing strategies contain further details [4], [5].

Although multi-primary configurations are associated with distributed scatterers, they are also beneficial for PS analysis. For example, multi-primary strategies can be used to expand the number of possible PS through the detection of “imperfect” PS in the quasi-PS (QPS) technique [8] and to counteract the effects of noisy primary images such as in the coherence pixel technique (CPT) [9] and stable point network (SPN) techniques [10], [11]. Such studies have rarely been analyzed in a more comprehensive framework relative to their contexts, however, nor have they closely examined how much redundancy should be introduced. Such generalizations are difficult since it is impossible to determine an analytical expression for  $A_{\text{all}}^+ C^+$ , and there are no standard metrics upon which to evaluate the quality of a multi-primary method.

Our focus here is to retrieve a more robust time-series result in a specific context—temporary PS decorrelation unrelated to long-term scattering changes. We use a multi-primary configuration to achieve these aims: first, by retaining only consistent PS candidates in all the primary image substacks; and second, by introducing redundancy in  $v$  using multi-primary substacks, then solving for  $v$  using the SVD-based inversion as in standard SBAS [6]. A flowchart of our method is shown in Fig. 1. Our configuration is simple and introduces additional redundancy and robustness in three distinct stages.

### III. SIMULATED DATA

We compared the performance of different pairing strategies using simulated data. We modeled a deformation sequence with a horizontal linear gradient spanning  $-6$  to  $-12$  mm/y

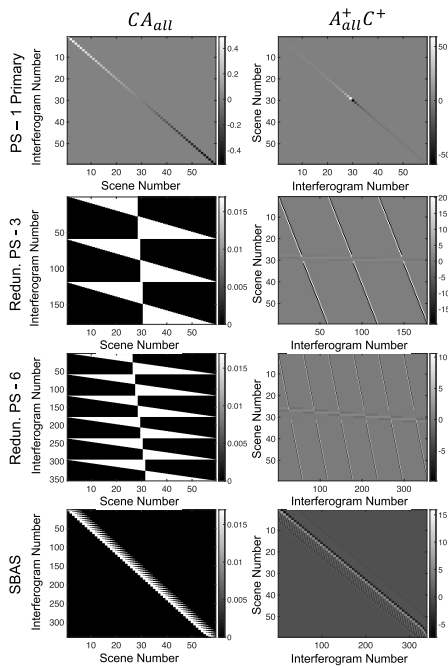


Fig. 2.  $CA_{\text{all}}$  and  $A_{\text{all}}^+ C^+$  for pairing strategies used in the simulations. For the single-primary case, the solution vector  $v$  was defined with respect to the primary image; for the multi-primary cases,  $v$  was defined with respect to the velocity between adjacent scenes.

over an image size of  $250 \times 250$  pixels. We assumed a high correlation for all the scatterers, with no temporal decorrelation other than a spurious decorrelation across six scenes, such that given the scene number  $i$ , the correlation  $\rho$  is defined

$$\rho = \begin{cases} 0.1, & \text{if } 7 \leq i \leq 12 \\ 0.9, & \text{otherwise.} \end{cases}$$

We assumed an imaging wavelength of  $\lambda = 0.6$  cm, a temporal revisit of 12 days, and negligible geometric baselines. We generated 60 scenes (spanning 720 days) and simulated the presence of thermal noise by adding standard normal-distributed random variables in both real and imaginary channels. In addition, we modeled a residual, uncorrected atmospheric signal with an rms value of 1 mm.

We tested four pairing configurations: PS-InSAR with one, three, and six primaries drawn from the chronological center of the stack, and a no-multilook SBAS configuration where we paired all the scenes separated by up to six other scenes. The corresponding  $CA_{\text{all}}$  and  $A_{\text{all}}^+ C^+$  are shown in Fig. 2. We solved for  $v$  using (2), and then used (5) to reconstruct the deformation sequence,  $d_{\text{est}}$ , which we referenced to a point deforming at the mean value of the original deformation sequence  $d_{\text{orig}}$ . To estimate (6), we computed the standard error of a linear fit to the deformation sequence by bootstrapping the residuals as in [12].

Fig. 3 shows the estimated cumulative subsidence and standard error for each pairing strategy. The original gradient and correlation patterns are also shown for reference. We found that the deformation pattern was retrieved more clearly with more primary images, and the mean standard error decreased as well. While the mean standard error appears low for the SBAS result, the estimated cumulative subsidence is clearly

much more dominated by atmospheric noise than any of the PS methods. Overall, we found that the original pattern was most faithfully retrieved with the R-6 configuration.

#### IV. CASE STUDY: TUTUILA, AMERICAN SAMOA

The island of Tutuila is the largest and most populated in American Samoa. Ongoing subsidence has been observed due to viscoelastic relaxation after the 2009 Samoa–Tonga earthquake [13]. For our case study, we compared the retrieved subsidence time-series using Sentinel-1 data with different pairing strategies, building upon results from Huang et al. [12] and the preliminary comparisons presented by Huang and Sauber showing the presence of spurious decorrelation on the island [14]. Correlation drops in our dataset are estimated to range in severity, spanning up to approximately 5% of interferograms and with estimated PS correlation dropping from values of 0.8 to 0.95 to anywhere between 0.2 and 0.7.

We analyzed all the scenes covering Tutuila between December 3, 2015, and August 16, 2022, and generated geocoded SLCs from L1 data using the Stanford InSAR System [15] to NASADEM, processing to its native resolution ( $30 \times 30$  m). We tested the same four pairing strategies as in the simulations: PS-InSAR with one primary (July 27, 2019), three primaries (July 3, 2019, July 27, 2019, and August 8, 2019), and six primaries (June 6, 2019–August 8, 2019), as well as SBAS. For SBAS processing, we found that no multilooking resulted in poor performance, so we upsampled the DEM by 2, took five looks in each direction, and formed all the interferograms with less than a 150-day baseline. The baseline plots are shown in Fig. 4. For multi-primary PS methods, we used a parametric non-Gaussian maximum likelihood PS detector [16], and for the single-primary method, we used the Gaussian variant [17] as the false-positive rate in this region was observed to be too high without multi-primary filtering. We masked the results from all the methods to the most restrictive PS set and selected the PS closest to the ASPA GPS station as our reference point. We calibrated results to the linear fit of subsidence at ASPA, using the Pacific fixed-plate solution from the University of Nevada Geodetic Laboratory [18], [19]. For atmospheric compensation, we used the power-law correction algorithm [20]. Finally, we computed cumulative subsidence rates with a linear fit to the time-series results at each PS. As validation, we compared the time-series to the VLM computed at the Pago Pago tide gauge station using the altimetry-tide gauge differencing (Alt-TG) method, which subtracts the absolute sea level measured by multisatellite altimetry from the relative sea level measured at the tide gauge station. The data and processing methodology are the same as that described in [12].

Fig. 5 shows the subsidence time-series derived from the Alt-TG method and InSAR. SBAS-derived perturbations are smaller than the R-1 case but greater than the R-3 case. Perturbations are significantly reduced when more primary images are used for PS-InSAR, with the R-6 case adhering most closely to the Alt-TG trends. The estimated cumulative subsidence rates and standard error for the tested pairing strategies are shown in Fig. 6. Consistent with our simulations, the standard error decreases from one to three to six primary



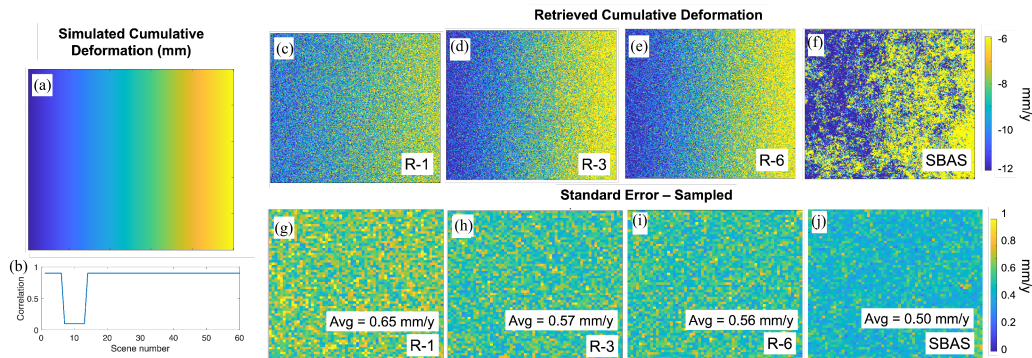


Fig. 3. (a) Deformation and (b) correlation patterns used in our simulations. We tested a horizontal gradient of  $-6$  to  $-12$  mm/y across an image of size 250 by 250 pixels, and all the pixels were simulated to have a correlation of 0.9 except for six scenes, from scene 7 to 12, inclusive, when correlation drops to 0.1. (c)–(f) Estimated cumulative subsidence rate using PS-InSAR with (c) one primary image (R-1); (d) three primary images (R-3); (e) six primary images (R-6); and (f) SBAS. (g)–(j) Corresponding standard error (due to computational heft, every fourth pixel displayed for representative summary).

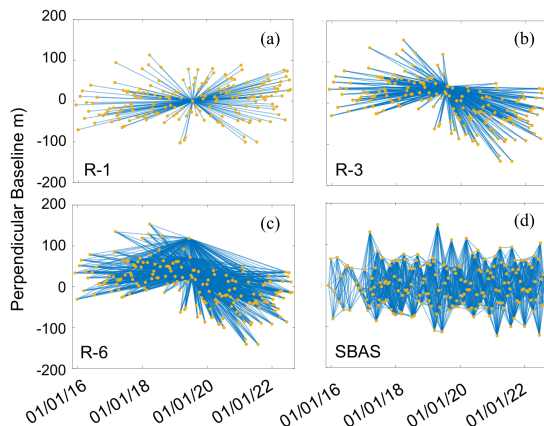


Fig. 4. Spatial and temporal baselines for pairing strategies used in our case study: (a) one primary image; (b) three primary images; (c) six primary images; and (d) SBAS. Our method imposes no baseline restrictions given PS resistance to decorrelation, but we still selected primary images in the chronological center of our dataset to reduce the possibility of PS disruptions over time.

images. The error rates for SBAS appear similar to those for the R-3 case for points close to the reference point, and similar to the R-1 case for points farther from the reference point. For PS-InSAR methods, in contrast, we observe a trend of improved error reduction with more primary images as the distance from the reference point at ASPA increases, and the estimated cumulative subsidence rates in the R-6 case are much less correlated with distance to ASPA compared with the R-1 case.

## V. DISCUSSION

Leveraging a multi-primary PS-InSAR configuration can clearly reduce time-series error in the presence of spurious decorrelation. There is evidence of further benefit beyond what we modeled in our simulations as well. While we observed no spatial trend in error reduction in our simulations, it was clear in our case study that error reduction was greater with increased distance from our reference point at the ASPA GPS station, with less observed near the reference point. This effect may be due to the fact that the reference point is located in the most densely settled area on Tutuila with the highest correlation, and correlation decreases in the more sparsely settled areas farther away from the reference point. This heterogeneity could also be due partly to the multi-primary

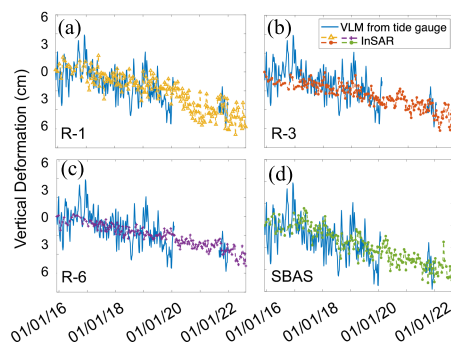


Fig. 5. Time-series comparison of subsidence at the Pago Pago station using the Alt-TG method (data unavailable from January 31, 2020, to September 2, 2021) and InSAR with (a) one primary image; (b) three primary images; (c) six primary images; and (d) SBAS. R-6 case performs best.

effects of reducing false positives and primary-dependent noise, which have been demonstrated in previous work but were not modeled in our simulations. These effects may also account for the variation in the average estimated cumulative subsidence rates that were observed in our case study but not in our simulations.

Several practical concerns should be considered when applying the method. First, primary images with the highest overall correlation should be selected; in our simulations, we observed no performance difference between selecting two scenes with the same correlation characteristics. Next, the number of primary images should be kept small, as computational redundancy increases for each image (in our unoptimized implementation, the computation time roughly doubled for each new primary image). In our simulations, we observed that the largest error reduction was associated with moving from a single-primary to a double-primary configuration, and error reductions became less pronounced as the number of primary images increased. However, in practice, we observed notable error reduction when more than two primary images were used (as shown in Fig. 6). Therefore, some experimentation may be necessary. Generally, we found that a reasonable guideline was to match the number of primary images with the approximate number of scenes containing spurious correlation drops, which must be estimated by analyzing a limited subset of PS as decorrelation trends can vary widely between datasets.



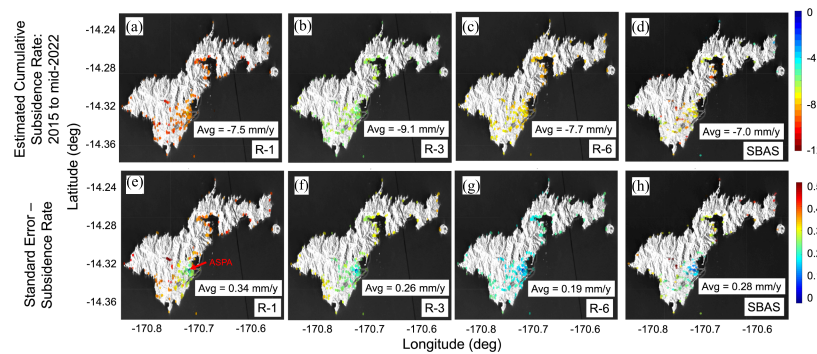


Fig. 6. Estimated cumulative subsidence rates on Tutuila using PS-InSAR with (a) one primary image; (b) three primary images; (c) six primary images; and (d) SBAS. (e)–(h) Corresponding standard error. Average error decreases from (e) to (f), with more error reduction at greater distances from the reference point (ASPA, marked in (e)). Accordingly, estimated cumulative subsidence rates in (c) appear much less correlated with distance from ASPA than in (a). SBAS shows no such trend, with error rates similar to the R-3 case close to ASPA and error rates similar to the R-1 case farther from ASPA.

Finally, we note that the technique is designed for large datasets, since it is more effective to manually inspect and drop troublesome scenes with a small number of SLCs. Thus, as many SLCs as possible should be used, given that PSs are resistant to temporal and spatial decorrelation by definition. In our simulations, increasing the number of SLCs used was only detrimental if the proportion of scenes exhibiting spurious decorrelation increased relative to correlated scenes.

## VI. CONCLUSION

We have demonstrated a multi-primary PS-InSAR pairing method that produces a more robust time series deformation in the presence of sudden, temporary decorrelation compared with standard PS-InSAR analysis. Our multi-primary method is simple in implementation and can measure low-to-moderate deformation rates under conditions that may be difficult to impossible for other InSAR methods. These increased capabilities will enable the estimation of rates of VLM in challenging coastal environments where knowledge of local trends in subsidence is key to developing effective resilience measures to the drastic consequences of sea level rise.

## ACKNOWLEDGMENT

The authors are grateful to Richard Ray for providing the processed Alt-TG data at the Pago Pago Tide Gauge. Tide gauge data were retrieved from the University of Hawaii Sea Level Center, and altimetry data were retrieved from the Data Unification and Altimeter Combination System (DUACS) delayed-time (DT-2021) product. Copernicus L1 Sentinel data 2015–2022 were accessed through the Alaska Satellite Facility Distributed Active Archive Center (ASF DAAC) from <https://asf.alaska.edu>.

## REFERENCES

- [1] D. P. S. Bekaert, B. D. Hamlington, B. Buzzanga, and C. E. Jones, "Spaceborne synthetic aperture radar survey of subsidence in Hampton Roads, Virginia (USA)," *Sci. Rep.*, vol. 7, no. 1, pp. 1–9, Nov. 2017.
- [2] M. Anzidei et al., "Relative sea-level rise scenario for 2100 along the coast of south eastern sicily (Italy) by InSAR data, satellite images and high-resolution topography," *Remote Sens.*, vol. 13, no. 6, p. 1108, Mar. 2021.
- [3] A. Martínez-Asensio et al., "Relative sea-level rise and the influence of vertical land motion at tropical Pacific islands," *Global Planet. Change*, vol. 176, pp. 132–143, May 2019.
- [4] B. Osmanoglu, F. Sunar, S. Wdowinski, and E. Cabral-Cano, "Time series analysis of InSAR data: Methods and trends," *ISPRS J. Photogramm. Remote Sens.*, vol. 115, pp. 90–102, May 2016.
- [5] D. Ho Tong Minh, R. Hanssen, and F. Rocca, "Radar interferometry: 20 years of development in time series techniques and future perspectives," *Remote Sens.*, vol. 12, no. 9, p. 1364, Apr. 2020.
- [6] P. Berardino, G. Fornaro, R. Lanari, and E. Sansosti, "A new algorithm for surface deformation monitoring based on small baseline differential SAR interferograms," *IEEE Trans. Geosci. Remote Sens.*, vol. 40, no. 11, pp. 2375–2383, Nov. 2002.
- [7] Y. Zheng, H. Zebker, and R. Michaelides, "A new decorrelation phase covariance model for noise reduction in unwrapped interferometric phase stacks," *IEEE Trans. Geosci. Remote Sens.*, vol. 59, no. 12, pp. 10126–10135, Dec. 2021.
- [8] D. Perissin and T. Wang, "Repeat-pass SAR interferometry with partially coherent targets," *IEEE Trans. Geosci. Remote Sens.*, vol. 50, no. 1, pp. 271–280, Jan. 2012.
- [9] P. Blanco-Sánchez, J. J. Mallorquí, S. Duque, and D. Monells, "The coherent pixels technique (CPT): An advanced DInSAR technique for nonlinear deformation monitoring," *Pure Appl. Geophys.*, vol. 165, no. 6, pp. 1167–1193, Jun. 2008.
- [10] M. Crosetto, E. Biescas, J. Duro, J. Closa, and A. Arnaud, "Generation of advanced ERS and ENVISAT interferometric SAR products using the stable point network technique," *Photogramm. Eng. Remote Sens.*, vol. 74, no. 4, pp. 443–450, Apr. 2008.
- [11] F. Kuehn et al., "Detection of land subsidence in Semarang, Indonesia, using stable points network (SPN) technique," *Environ. Earth Sci.*, vol. 60, no. 5, pp. 909–921, May 2010.
- [12] S. A. Huang, J. M. Sauber, and R. Ray, "Mapping vertical land motion in challenging terrain: Six-year trends on Tutuila Island, American Samoa, with PS-InSAR, GPS, tide gauge, and satellite altimetry data," *Geophys. Res. Lett.*, vol. 49, no. 23, pp. 1–10, Dec. 2022.
- [13] S. Han, J. Sauber, F. Pollitz, and R. Ray, "Sea level rise in the samoan islands escalated by viscoelastic relaxation after the 2009 Samoa-Tonga earthquake," *J. Geophys. Res., Solid Earth*, vol. 124, no. 4, pp. 4142–4156, Apr. 2019.
- [14] S. Huang and J. Sauber, "Successes and challenges of MT-InSAR methods in coastal regions: A case study on the Island of Tutuila, American Samoa," in *Proc. IEEE Int. Geosci. Remote Sens. Symp.*, Mar. 2023, pp. 3998–4001.
- [15] H. Zebker, "How to process your InSAR time series with the Stanford InSAR system," Presented at the NISAR Sci. Community Workshop, 2022.
- [16] S. A. Huang and H. A. Zebker, "InSAR time-series analysis with a non-Gaussian detector for persistent scatterers," *IEEE J. Sel. Topics Appl. Earth Observ. Remote Sens.*, vol. 15, pp. 9208–9225, 2022.
- [17] P. Shanker and H. Zebker, "Persistent scatterer selection using maximum likelihood estimation," *Geophys. Res. Lett.*, vol. 34, no. 22, Nov. 2007, Art. no. L22301.
- [18] F. E. Marion, G. Sella, and M. Hayward, "ASPA." Nat. Ocean. Atmos. Admin., Washington, DC, USA, 2001. [Online]. Available: <https://geodesy.noaa.gov/corsdata/>
- [19] G. Blewitt, W. Hammond, and C. Kreemer, "Harnessing the GPS data explosion for interdisciplinary science," *EOS*, vol. 99, pp. 1–10, Sep. 2018.
- [20] D. P. S. Bekaert, A. Hooper, and T. J. Wright, "A spatially variable power law tropospheric correction technique for InSAR data," *J. Geophys. Res., Solid Earth*, vol. 120, no. 2, pp. 1345–1356, Feb. 2015.